Robust and Versatile Light Absorption at Near-Infrared Wavelengths by Plasmonic Aluminum Nanorods

Olivier Lecarme, Quan Sun, Kosei Ueno, and Hiroaki Misawa*

Research Institute for Electronic Science, Hokkaido University, Sapporo, 001-0021, Japan

Ⓢ Supporting Information

ABSTRACT: We investigate the far-field and near-field properties of aluminum nanorods fabricated by electron beam lithography and exhibiting plasmonic resonance in the near-infrared region. First, we show that plasmonic modes within nanorod arrays can be tuned by geometrical parameters, allowing one to control the system transparency. Next, the light absorption in this structure is closely examined, and we demonstrate that aluminum has great potential due to its unique interband transition at 800 nm. The roles of the dielectric confinement and the coupling between plasmonic resonance and the interband transition are particularly emphasized, as their adjustment can be used to switch from highly scattering particles to absorbing particles without a significant modification of the plasmonic resonance position. Finally, we image the plasmon-generated local field distribution in the aluminum nanostructures and observe, for the first time, the effect of the interband transition on the near-field behavior. The effect of the dielectric confinement is also numerically investigated, as it is shown to play a significant role in near-field enhancement.

KEYWORDS: plasmonics, aluminum, near-infrared, interband transition, near-field enhancement, photoemission electron microscopy
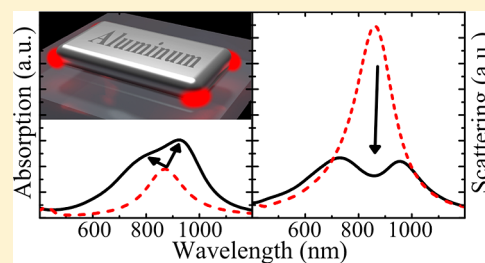
Over the past decade, metallic nanostructures have been extensively studied due to their plasmonic properties. Although the visible region has received the most attention, plasmonic systems working in the near-infrared (near-IR) region, wavelengths from 700 nm to a few micrometers, have received increasing interest due to their potential applications in various fields. The near-IR region corresponds to the transparent window of the majority of living tissues.[1] These structures are, thus, particularly well-adapted for noninvasive and nondestructive medical diagnosis[2,3] and treatment.[4,5] In the field of solar energy, the near-IR region is also very attractive, as 45% of the total solar intensity is located between 750 nm and 1.75 μm.[6] Plasmonic nanoparticles have been successfully employed to improve the light-harvesting efficiency in this spectral area using silicon-based solar cells.[7−9] Near-IR photocurrent generation[10] and water oxidation[11] have also been recently reported using gold (Au) nanorods.

Au and silver (Ag) are the two most commonly used materials in plasmonics, as they show strong optical resonance and are easy to handle. However, these materials are expensive and are limited resources. Aluminum (Al) has recently been presented as a potential low-cost alternative to noble metals, as it can support localized surface plasmon resonance (LSPR) from deep UV to IR wavelengths.[12−18] Beyond its cost-effectiveness, Al exhibits unique optical characteristics. First, its almost Drude-like behavior enables LSPR stability for shorter wavelengths (down to ~150 nm) than Au (~500 nm) and Ag (~345 nm). Additionally, the light absorption efficiency is expected to be high in the near-IR region, as interband transitions (ITs) occur in that region.[19] As evidence of the growing interest in this material, Al nanoparticles[20] and disks[21,22] have recently been shown to increase the photocurrent in silicon photodiodes by means of the LSPR light-scattering effect.

In this study, we examine the optical properties of Al nanorods fabricated on a high-refractive-index, transparent substrate. We present a complete experimental and theoretical investigation of the far-field and near-field behavior in the near-IR region, with a focus on three key physical quantities. First, the tuning of the LSPR position is examined as a function of the structure's geometrical parameters. Second, the absorption and scattering efficiency of the Al nanorods are investigated in detail. Particular attention is given to the IT region, as these transitions are known to strongly interfere with the LSPR when their energies overlap.[23] The role of the geometrical parameters, particularly, the particle volume, is also explored. We show that the structure's shape can be optimized to create strong light-harvesting nanosystems, resulting from an improvement in the absorption efficiency combined with a suppression of the scattering efficiency. Third, the local near-field wavelength dependence is measured using photoemission electron microscopy (PEEM) to evaluate the effect of the ITs on the plasmon-excited local electric field. The experimental results are combined with theoretical investigations on near-field enhancement and its relationship to the geometry of the nanostructures.
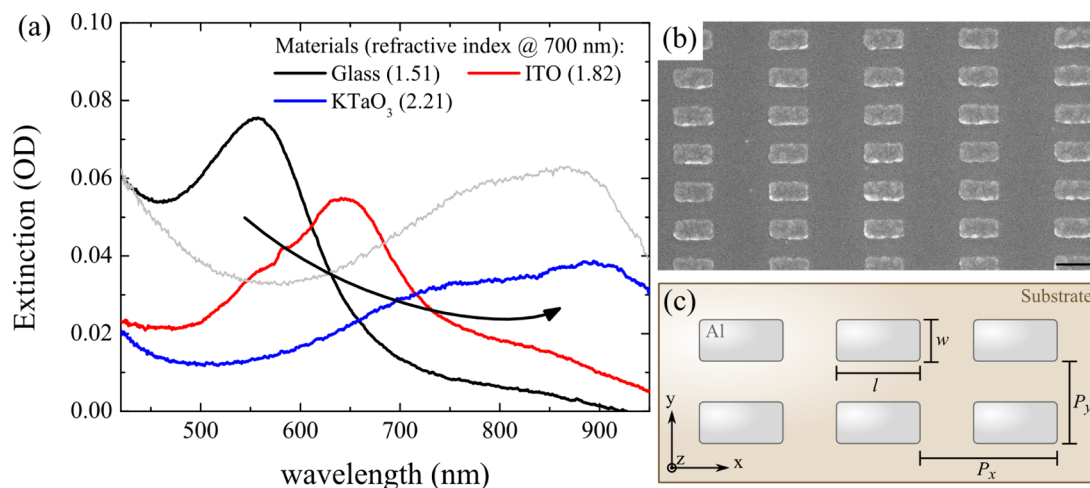
Figure 1. (a) Experimental extinction spectra of 130 × 65 nm Al nanorods on different substrates. Rods with dimensions of 180 × 90 nm² on glass (light gray curve) are included for comparison. (b) SEM micrograph of a thin Al nanorod array on KTaO₃. Scale bar: 200 nm. (c) Schematic view of the geometry of the structures.

■ TUNING OF THE PLASMON RESONANCE

Ordered arrays of 20 nm thick Al nanorods were fabricated using electron beam lithography and metal evaporation techniques. To obtain LSPR in the near-IR region without significant contributions from multipolar plasmonic resonances, a high-refractive-index material was chosen as a substrate. As shown in Figure 1a, due to an intermediate mediated redshift,[24−26] the use of a KTaO₃ substrate allows for LSPR at long wavelengths, between 700 and 900 nm, with relatively small nanorods (130 × 65 nm²). As a comparison, 180 nm long nanorods are required to achieve LSPR in the same wavelength range when using a glass substrate. The contribution of multipolar orders increases with the size of the structures; thus, their role is significantly reduced by using a high-refractive-index substrate, leading to systems with less complex optical characteristics. Thus, in this study, nanostructures were fabricated on single-crystal KTaO₃ [100] (Figure 1b), a transparent material in the visible and near-IR region with a refractive index of approximately 2.2. Strong broadening was observed for the LSPR at approximately 800 nm, which is related to the specific IT of the Al and will be studied in detail hereafter.

The role of the geometrical parameters of these systems, such as the length l, the aspect ratio l/w (width), and the array pitch (P_x; P_y) in determining the structure's optical behavior was investigated (Figure 1c). When not explicitly specified, the pitches were chosen to be $P_x = P_y = 2.5l$ to avoid near-field interactions.

First, the optical properties of nanorods with lengths ranging from 130 to 230 nm were studied. The aspect ratio was fixed at $l/w = 2$ for all sizes. Under unpolarized illumination, a redshift of both the longitudinal (L) and transversal (T) modes can be observed (Figure 2a). A linear redshift of the L-mode LSPR peak position is observed and can be fit with the following relation: $\lambda_{LSPR} = 301 + 4.48l$ (coefficient of determination $R^2 = 0.98$). This trend indicates that these structures are in a material-independent regime, where the LSPR position is primarily determined by the geometry of the object, with a negligible contribution of the material.[15] This behavior arises from the length of the nanorods, which is much larger than a dipolar particle (size < 20 nm).
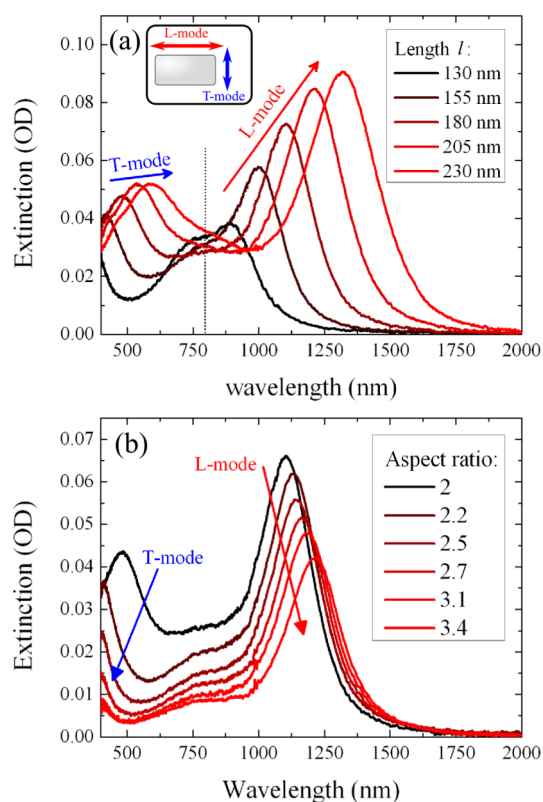

Figure 2. Experimental extinction spectra of (a) size-variable Al nanorods with the aspect ratio l/w maintained at 2 and (b) Al nanorods with increasing aspect ratio (length maintained at $l = 180$ nm).

The effect of the aspect ratio was also measured while the nanorod length was fixed at $l = 180$ nm (Figure 2b). Narrower rods exhibited an increased electronic confinement, which induces an exponential redshift of the L-mode in this configuration: $\lambda_{LSPR} = 1094 + 0.1 \exp(2.44l/w)$ ($R^2 = 0.99$). At the same time, the T-mode shifts toward the UV region. Because both modes move away from the visible window as the aspect ratio increases, that latter can be used to tune the transparency of the material.
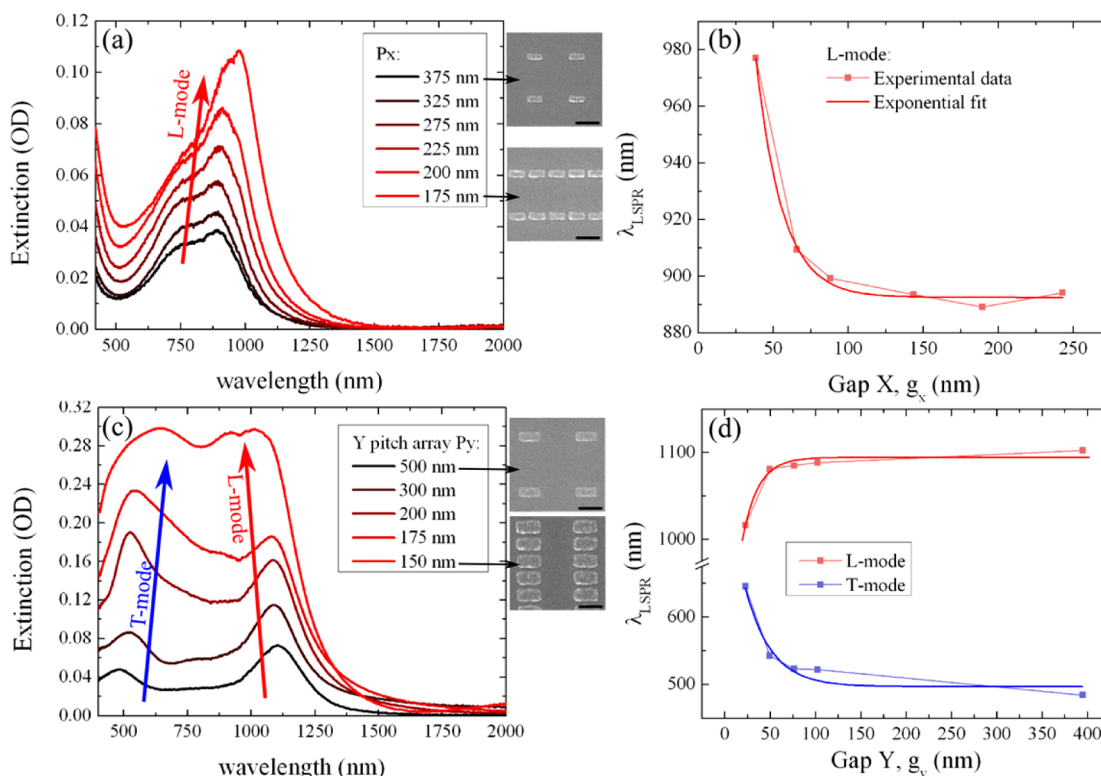
Figure 3. (a) Experimental extinction spectra of 130×65 nm^2 nanorods for decreasing array pitch along the x-axis P_x and (b) evolution of the corresponding L-mode position. The X gap is $g_x = P_x - l$. (c) Experimental extinction spectra of 180×90 nm^2 nanorods for decreasing array pitch along the x-axis P_y and (d) evolution of the corresponding L- and T-mode positions. The Y gap is $g_y = P_y - w$. Scale bar of the SEM pictures: 200 nm.

The pitch of an ordered array of metallic nanostructures is also known to alter the LSPR characteristics, particularly due to far-field interference and diffraction effects.[27,28] In high-density arrays, when the particle-to-particle distance is on the same order of magnitude as the nanorod size, near-field interactions are expected to be significant. Because a nanorod is a two-axis structure, the effects of particle interdistance, or the gap, along the main axis (g_x) and perpendicular to it (g_y), were investigated.

When a decrease in the gap along the x-axis is considered (Figure 3a,b), an exponential redshift of the L-mode position arises: $\lambda_{\mathrm{LSPR,L}}(g_x) = A \exp(-g_x/d) + \lambda_0$ (fit parameters are shown in Table 1). This behavior is similar to that observed for

Table 1. Exponential Fit Parameters Used in Figure 3b,d

key parameter	A (nm)	d (nm)	y_0 (nm)	R^2
gap g_x, L-mode	759	17.5	892	0.99
gap g_y, T-mode	497	28.4	497	0.92
gap g_y, L-mode	−292	17.3	1094	0.94

metallic dimers[29−32] and is thus related to a near-field plasmonic coupling. Indeed, the exponential dependence on gap size is known to arise from the contribution of each multipolar LSPR order to the total evanescent field intensity distribution at the edge of a particle.[33] If the gap along the y-axis (Figure 3c,d) is considered, a similar behavior is observed for the T-mode: $\lambda_{\mathrm{LSPR,T}}(g_y) = A \exp(-g_y/d) + \lambda_0$ (fit parameters in Table 1), which is directly affected by the Y gap. Similar to dimer systems, the L-mode, which is perpendicular to the Y gap, shifts to lower wavelengths. However, the shifting

amplitude is high, with a 78 nm shift to the asymptotic value for $g_y = 25$ nm instead of ∼25 nm, as would be observed in the dimer case for a similar gap value.[30,34] We suggest that this difference may arise from far-field diffraction or long-range plasmonic effects,[35] which are expected to play a significant role in our structures. Alternatively, the wide edge-to-edge surface in this case may alter the interactions between the two parallel L-modes.

To summarize, changes in g_x and g_y exert opposing effects on the LSPR position. Thus, a controlled simultaneous reduction of these gaps can allow one to maintain the LSPR at the same wavelength as the array density is increased. Furthermore, this effect can be used, as found for the aspect ratio, to control the transparency of the material.

■ LIGHT ABSORPTION

To monitor the absorption efficiency in the near-IR region and to evaluate the key parameters influencing this efficiency, finite-difference time-domain (FDTD) calculations were performed. The dimensions of the modeled systems were chosen to match the previously fabricated structures and are given in the Supporting Information.

The calculated extinctions for five sizes of Al nanorods were compared with experimental data (Figure 4a). Very good agreement is observed between the experimental and modeling results for both the LSPR position and width. The additional peak observed at lower wavelengths in the experimental data arises from the excited T-mode under unpolarized illumination, which was not included in the calculations, as it is far from the near-IR region. When the LSPR is close to 800 nm, significant broadening of the extinction peak is observed. If we focus on
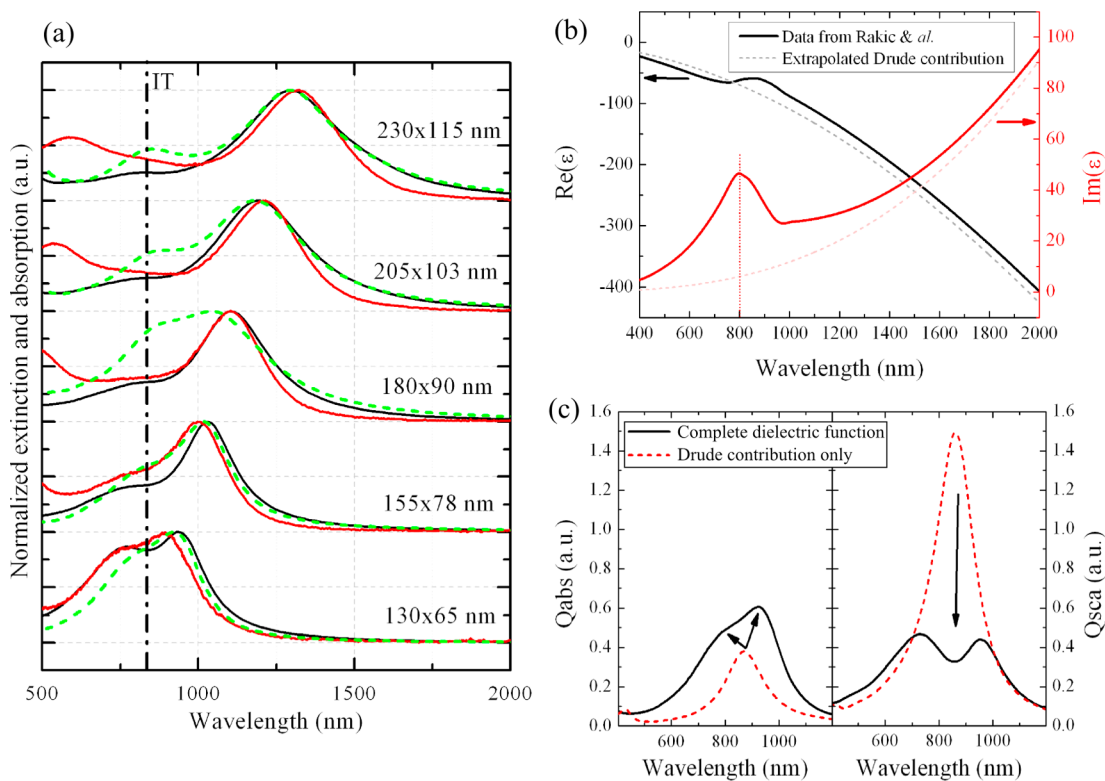
Figure 4. (a) Normalized experimental extinction (red curves) of size-variable Al nanorods under unpolarized light and corresponding extinction (black curves) and absorption (green dashed curves) calculated by FDTD for L-polarization. (b) Dielectric function of Al from Rakic's data[36] and extrapolated Drude term of the dielectric function, with ω_p = 13.1 eV, γ_c = 132 meV, G_0 = 15, ω_0 = 1.64 eV, and Γ = 707 meV. (c) Calculated absorption and scattering cross-section of 130×65 nm^2 Al nanorods based on the dielectric functions presented in (b).

the absorption component only (Figure 4a, green dashed curves), a second peak is always visible near this wavelength. In fact, Al is a nearly free-electron metal and a lossy material compared to noble metals,[37] with an interband transition (IT) between two parallel bands[19] ($\Sigma_3 \to \Sigma_1$ in the $\Gamma-K$ Brillouin zone) leading to additional absorption at 800 nm (1.55 eV). This interband process involving valence electrons does not persist at higher energies as it does for noble metals, such as Au, Ag, and Cu, and is the only significant process for wavelengths longer than 157 nm. This behavior results in a single absorption peak visible in the imaginary part of the dielectric function of Al (Figure 4b). The second peak observed in the absorption spectra shown in Figure 4a results from coupling between the LSPR and the single, energy-localized IT of Al.[15] The enhancement in optical absorption induced by this strong interaction has been calculated by Pakizeh[38] and has been described as a dipole–dipole interaction (in the quasistatic limit) leading to two new hybridized modes. The resulting repulsive noncrossing energy behavior between the LSPR and the IT has recently been experimentally confirmed in Al films with nanoholes.[23]

To identify the contribution of the IT to the total optical absorption, the spectral properties of the nanorods were simultaneously calculated using the dielectric function ε of Al measured by Rakic[36] and the extracted Drude contribution only, ε_{Drude}. To separate the free electron (or Drude) behavior and the interband component, we fit the real and imaginary part of the measured ε with a Drude-Lorentz model, expressed here as a function of the frequency ω:

$$\varepsilon(\omega) = \varepsilon_{Drude}(\omega) + \varepsilon_{IT}(\omega)$$

$$= \left[1 - \frac{\omega_p^2}{\omega(\omega + i\gamma_c)} \right] + \left[\frac{G_0\omega_0^2}{\omega_0^2 - \omega^2 - i\Gamma\omega} \right] \quad (1)$$

ω_p and γ_c are the plasma frequency and the collision rate. G_0, ω_0, and Γ are, respectively, the gain, the central wavelength of the IT, and its related damping factor. The fit values obtained for the Drude part (ω_p = 13.1 eV, γ_c = 132 meV) are in good agreement with the literature.[39] The resulting pure Drude dielectric function is displayed and compared with the complete function in Figure 4b.

To monitor the absorption efficiency of the Al nanostructures, the absorption (Q_{abs}) and scattering (Q_{sca}) cross sections were simultaneously calculated. Figure 4c shows Q_{abs} and Q_{sca} for 130×65 nm^2 Al nanorods based on ε and ε_{Drude}. The results show that the addition of the IT contribution induces a split in the absorption peak and an increase in its maximum intensity. This hybridization behavior, resulting from the coupling between the LSPR and the IT, is in perfect accordance with the study reported by Pakizeh.[38] Conversely, the scattering is significantly quenched, with the appearance of a dip in the peak and an almost 4-fold reduction in the maximum intensity. The ratio between Q_{abs} and Q_{sca} is thus completely reversed by the presence of the IT.

The results were also compared with those of Au structures of the same size, as a reference material that is commonly used in plasmonics (Figure 5a). For the "Drude Al" case, due to the large dimensions of the structures ($l \gg 20$ nm), the scattering component is clearly larger than the absorption component in the Au nanorod. In fact, the ratio between the light absorption
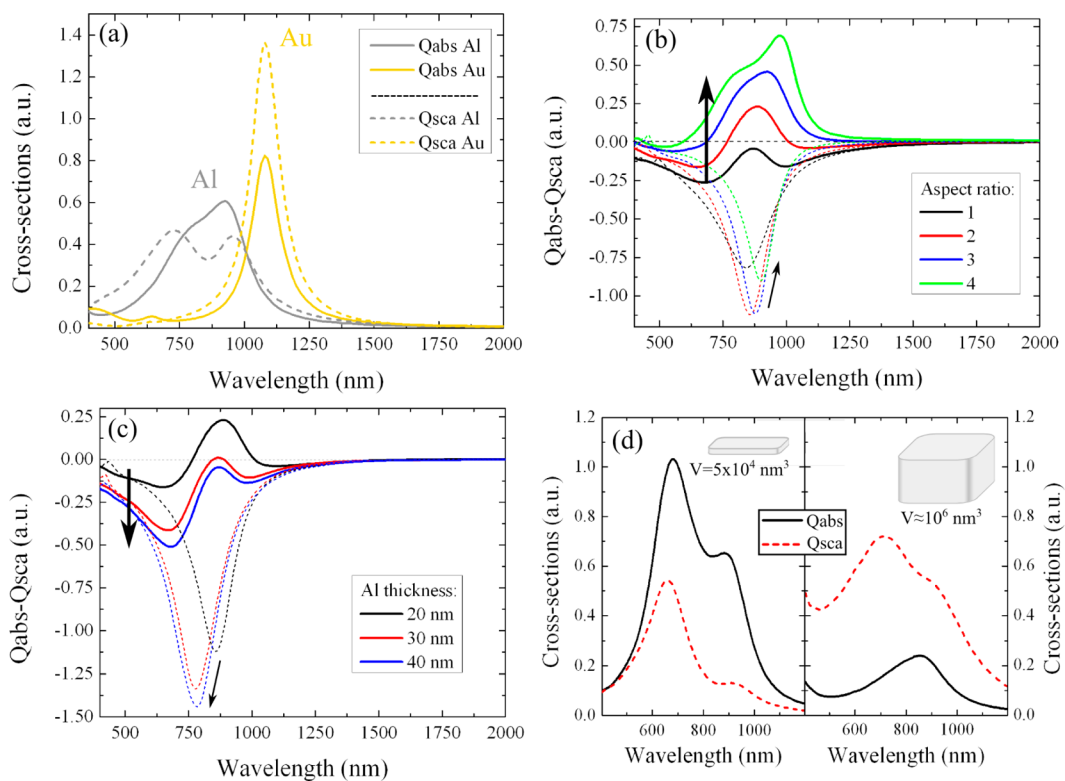
Figure 5. Theoretical investigation of Q_{abs} and Q_{sca}: (a) Comparison of Q_{abs} and Q_{sca} for 130×65 nm^2 nanorods composed of Au and Al. (b, c) Difference between Q_{abs} and Q_{sca} for increasing aspect ratio (length of 130 nm) and thickness (130×65 nm^2 nanorods), respectively. The solid curves show results based on the complete dielectric function of Al, and the dashed curves indicate the results calculated for the Drude component only. Raw data are available in Supporting Information, Figure S1. (d) Optical behavior of Al nanorods ($100 \times 25 \times 20$ nm^3) and nanoblocks ($130 \times 130 \times 60$ nm^3) with optimized absorption or scattering efficiency, respectively, in the near-IR region.

and scattering is known to decrease with size in metallic nanoparticles. Indeed, following from the electromagnetic formalism in the quasistatic approximation, the scattering and absorption cross sections of a sphere are given by[40]

$$Q_{abs} = 4x \, \mathrm{Im} \frac{\varepsilon - \varepsilon_m}{\varepsilon + 2\varepsilon_m}, \quad Q_{sca} = \frac{8}{3} x^4 \left| \frac{\varepsilon - \varepsilon_m}{\varepsilon + 2\varepsilon_m} \right| \quad (2)$$

$x = 2\pi\varepsilon^{1/2} r/\lambda$ and ε_m are, respectively, the size parameter of a sphere of radius r and the dielectric function of the surrounding medium. From these formulas, we can deduce the resulting relation between the absorption-to-scattering ratio and the particle volume V:

$$\frac{Q_{abs}}{Q_{sca}} \propto \frac{1}{x^3} \propto \frac{1}{V} \quad (3)$$

As this relation is also true for ellipsoids,[41] it is reasonable to suggest that it can be applied to our geometry. If we suppose that this relation is also extendable to the nondipolar case, the absorption efficiency could then be improved by increasing the dielectric confinement, that is, by reducing the volume. In the present study, the length of the nanorods was fixed to 130 nm to confine the longitudinal LSPR to the near-IR region. Thus, the effect of a volume reduction was investigated based on the aspect ratio and thickness of the nanostructures.

For clarity, the difference between the absorption and scattering cross sections was considered instead of their ratio. First, $Q_{abs} - Q_{sca}$ was calculated for 130 nm long Al nanostructures with geometry ranging from a square shape (aspect ratio = 1) to a narrow rod (aspect ratio = 4) using both

ε and ε_{Drude} only as the dielectric function. When real Al material is considered, the results in Figure 5b show that the square structures are dominated by the scattering component ($Q_{abs} - Q_{sca} < 0$). As the aspect ratio increases, the absorption peak near the IT position becomes increasingly significant. Calculations for 130×65 nm^2 rods with different thicknesses (from 20 to 40 nm) give similar results (Figure 5c). For 30 and 40 nm thick rods, scattering is the primary contribution to the total extinction, but for 20 nm thick rods, the absorption component increases dramatically at approximately 800 nm.

For the "Drude Al" case, the behavior remains the same, with an increase in the absorption-to-scattering ratio upon volume reduction, except for the square geometry. However, the observed change is weaker in comparison to the real Al case, where the IT is considered. Consequently, we suggest that the dielectric confinement may not be sufficiently strong to counter the effect of the quadrupolar contribution, which is expected to be significant for the square shape. As the quadrupolar mode is nonradiative, it may thus result in additional absorption, leading to a higher absorption-to-scattering ratio in comparison to the nanorod geometry.

Except for the square shape, similar behaviors for the cross-section ratio and volume were obtained for Au nanorods (see Figure S2 in the Supporting Information). Thus, the dielectric confinement is a significant factor in the evolution of the absorption and scattering intensity for our nanostructures. Nevertheless, the IT seems to play a more critical role, as its presence allows one to obtain $Q_{abs} > Q_{sca}$ for almost all wavelengths in the case of a high-aspect-ratio rod and as it

overwhelms the effects of potential multipolar contributions in the square geometry.

The strong impact of the LSPR-excited IT can be explained by using an analogy to quantum electrodynamics cavity systems. Indeed, the coupling efficiency is known to improve with the quality factor of the cavity (related to the photon lifetime) and with decreasing volume (spatial confinement). Yet, the quality factor of the LSPR significantly increases with the aspect ratio of nanorods due to a decrease in the dephasing rate.[42] Simultaneously, the mode volume is reduced. The global efficiency of the cavity is then greatly improved, providing a stronger resonant interaction between the LSPR and the IT and extended absorption. These considerations are in accordance with the observed peak position evolution of both the LSPR and the IT as the aspect ratio increases. Indeed, the IT appears to be blueshifted, even though the LSPR redshifts faster than its equivalent for the Drude case (see Supporting Information, Figure S3). Consequently, the repulsion of the LSPR and IT energy is increased, which corresponds to an improvement in their coupling.

We demonstrated that the cross-section ratio can be precisely tuned in the near-IR region by changing the dielectric confinement of the structures. For high absorption efficiency, the ideal structures should be thin, narrow nanorods. As an example, optical cross sections of an optimized design are shown in Figure 5d. A rod with dimensions of $100 \times 25 \times 20$ nm^3 was chosen because its optical response at each wavelength is dominated by absorption and because it can be built using conventional nanofabrication techniques while still supporting LSPR near 800 nm.

In contrast, a thick square nanoblock is the most adaptive geometry for such a system, as it can achieve a low absorption-to-scattering ratio (Figure 5d). Because no "parasitic" losses, that is, interband damping, are present below 700 nm, as observed for Au and Ag, such structures could be used in systems requiring broadband scattering properties in the visible region.[22]

■ NEAR-FIELD ENHANCEMENT

To monitor the near-field distribution, measurements were first performed using photoemission electron microscopy (PEEM). This technique has previously been employed to map the plasmon-enhanced electric field in Ag nanoparticles[43] and, more recently, in different geometries of Au nanostructures.[44,45] In the latter case, LSPR excited by ultrashort laser irradiation can induce multiphoton photoemission processes in correlation with the local electric field intensity.

For this study, length-variable Al nanorods were fabricated on ITO, as a conductive substrate is required to avoid charge accumulation during the experiments. Figure 6a shows a sample photoemission image obtained from an array of 190×95 nm^2 Al nanorods illuminated at the LSPR wavelength. The electrons involved in LSPR are known to be located at the surface of the metal only. However, a signal can still be collected in our case, despite the presence of the 3−4 nm thick native oxide layer covering the Al nanostructures.[46] The maximum photoemission is always observed at the corners of the rods, as expected from optical calculations (inset of Figure 7a), showing that the plasmon-enhanced electric field generated from the metallic structures is truly observed. We assume that the gradient of the electric field resulting from the plasmon resonance is strong enough to favor electron tunneling. Additionally, considering the peak power of the laser illumination (135 MW·cm^{-2}), the
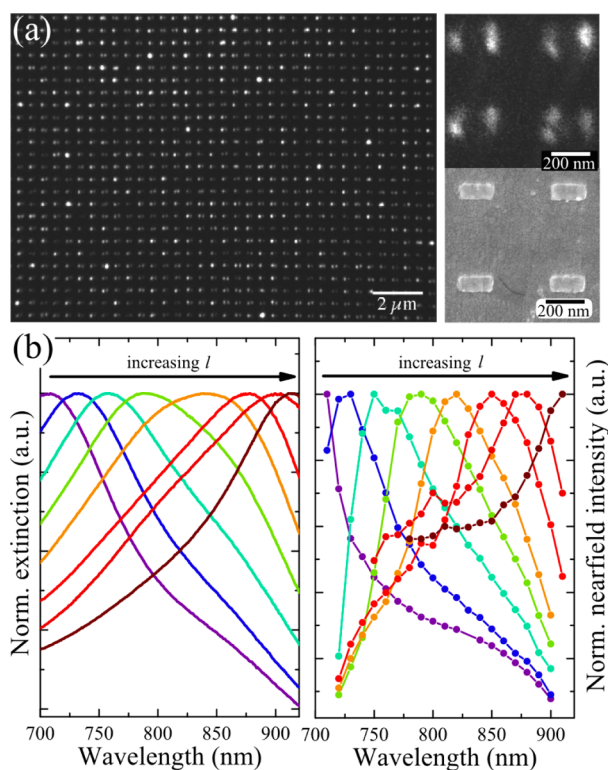

Figure 6. (a) PEEM image of a 190×95 nm^2 Al nanorod array under 800 nm illumination: (left) wide field of view, (top right) high-magnification view of 4 nanorods, and (bottom right) corresponding SEM micrograph. (b) Measured far-field extinction spectra and corresponding near-field intensity spectra for Al nanorods with increasing length l = 160, 170, 180, 190, 200, 210, 220, and 230 nm. The rod's aspect ratio is kept at 2.

local heating induced by the plasmonic near-field focusing[47] could generate cracks in the oxide layer and could thus create paths for electrons.

To obtain near-field spectra, the Al nanorod array near-field intensity was imaged and integrated over a 30 μm wide circular field of view, step-by-step, for illumination wavelengths ranging from 710 to 910 nm. To correct for the nonlinear dependence on wavelength (which induces a deformation of the spectral shape), the nonlinear order was extracted from power-dependence measurements at different wavelengths (between 3 and 5.5 photon processes were measured), and a correction was applied to the near-field spectra. Calculations and experimental curves are detailed in the Supporting Information (Figure S4). The resulting near-field spectra are presented in Figure 6b and are compared with their corresponding extinction spectra. The far- and near-field results are remarkably similar. The LSPR redshift induced by the increase in nanorod length can be seen in both cases, and the peak positions in the near-field are almost the same as those in the far-field, with a difference $\Delta\lambda$ = 13 ± 10 nm. As previously demonstrated, the broadening of the extinction curves, resulting in an elongation of the right side of the peak when $\lambda_{LSPR} < 800$ nm and of the left side for longer resonances, arises from the resonant interaction between the LSPR and the IT. Similar behavior was clearly observed for the near-field spectra. Thus, the direct effect of the IT on the local electric field is observed for the first time, to our knowledge, in plasmonic nanostructures. Considering the remarkable similarity between the far-field and near-field spectra as well as the relative thinness of the
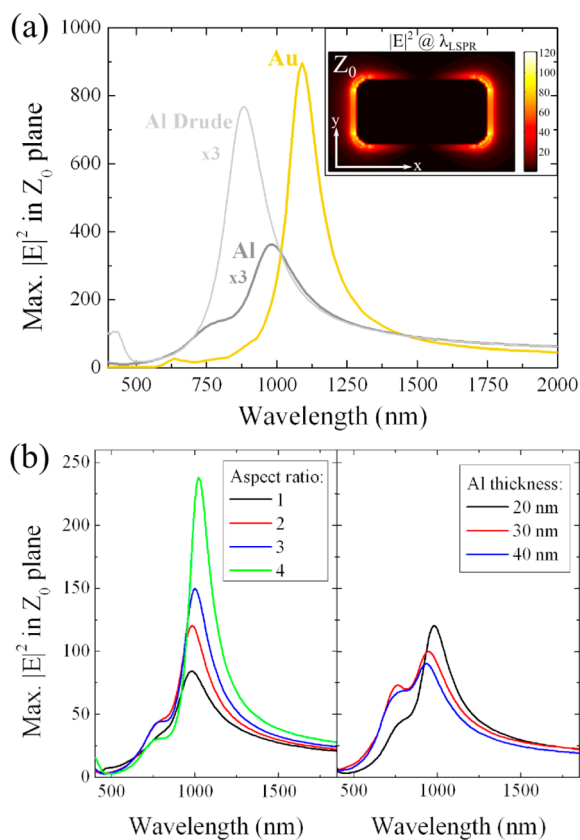
Figure 7. (a) Calculated electric field enhancement of 130×65 nm^2 Al, Au, and Drude-like Al nanorods. Inset: corresponding electric field distribution map for Al at the substrate interface (Z_0 plane). (b) Calculated electric field enhancement for different aspect ratios (thickness kept at 20 nm) and different thicknesses (aspect ratio kept at 2) in Al nanorods with $l = 130$ nm.

near-field peaks, we propose that the local electric field is also strongly coupled with the IT. The nature of the LSPR-IT interaction may be comparable to the one inducing strong coupling and Rabi splitting in plasmon/exciton systems like metallic nanostructures covered by J-aggregate.[48,49] Indeed, in addition to a close far-field behavior, the relation between far-field and near-field noticeable from our experimental data (Figure 6b) is also observed by Schlather et al.[50] on Au dimers/J-aggregate nanostructures. They show a correlated evolution of the near-field enhancement intensity and the scattering intensity of one hybrid mode peak, confirming that the coupling efficiency depends directly to the near-field enhancement.

To evaluate the absolute near-field intensity of the Al nanorods, field distribution maps were calculated for the same systems used in the absorption study. The normalized electric field intensity is defined as $|E|^2 = |E_{tot}|^2/|E_{inc}|^2$, where E_{tot} is the total electric field and E_{inc} is the incident electric field. The intensity distribution at the Al/substrate interface (plan Z_0) was investigated in detail, as the greatest electric field localization and intensity arise at the corners of the rods (inset of Figure 7a). The near-field enhancement spectra were calculated from the maximum of $|E|^2$ extracted at each wavelength.

Figure 7a shows the results for Al, Drude Al, and Au nanorods with the same size (corresponding to the far-field spectra in Figure 6a). The Al structure exhibits a 5-fold weaker enhancement in comparison to Au because of its "lossy" nature.

In particular, the IT induces quenching of the local field at approximately 800 nm, leading to a 2-fold decrease in the maximum intensity. Additionally, our calculations show that the native oxide surrounding the nanorods contributes to the overall reduction of the near-field enhancement, which decreases by a factor of 1.5 when an Al$_2$O$_3$ layer is added to a pure Al structure (Figure S5 in the Supporting Information).

As the dielectric confinement increased, the near-field enhancement also increased (Figure 7b), as observed for the absorption. A higher aspect ratio induces a significant improvement, with a maximum intensity $3\times$ higher for $l/w = 4$ than for the square shape. A similar trend was observed as the thickness was reduced, but the results were not as pronounced as for the aspect ratio (1.3-fold increase as the thickness decreases from 40−20 nm). We suggest that the increase in the LSPR quality factor leads to a stronger localization of the electric field, thus, allowing higher intensities to be reached. Additionally, as the LSPR position is shifting away from the IT as the aspect ratio increases, the overall contribution of the IT on the LSPR damping is reduced favoring high field enhancement (Figure S6 in the Supporting Information). Although the improvement in the LSPR-IT coupling is expected to reinforce the LSPR damping it does not seem to notably affect the nearfield behavior in that case.

Although this near-field improvement is appreciable, more advanced geometries could also be employed to more strongly amplify the near-field. For example, metallic dimers with a nanometric gap exhibit strong field localization between the two particles.[51−53] FDTD calculations performed for an Al dimer with a 1 nm gap show a maximum intensity reaching 5.7 $\times 10^4$ (e.g., almost $700\times$ the single block value). More detailed results regarding Al dimers are displayed in Supporting Information, Figure S7.

■ CONCLUSIONS

We have shown that Al nanorods fabricated on high-refractive-index material have a well-defined LSPR in the near-IR region. The positions of both the L- and T-modes can be precisely tuned by changing the size, the aspect ratio, and the interspacing distance of the rods.

Additionally, calculations on these systems demonstrated that Al is an ideal material for light absorption in the near-IR region, as the plasmon-excited IT significantly increases the efficiency at approximately 800 nm. Moreover, the absorption-to-scattering ratio can be significantly modified by changing the dielectric confinement, that is, the width and thickness of the rods, to favor either scattering or absorption, due to the modification of coupling strength between the LSPR and the IT. That coupling, specific to Al, especially offers the possibility to reach higher absorption-to-scattering value than Au for the same configuration (e.g., 1.3$\times$ higher for $130 \times 32.5 \times 20$ nm^3 nanorods) on a much broader spectral range (e.g., 2.7$\times$ wider fwhm for $130 \times 32.5 \times 20$ nm^3 nanorods).

Finally, local electric field distributions were experimentally obtained, and we observed, for the first time, direct interference between the IT and the plasmonic near-field. Using calculations, we showed that even if the enhancement intensity remains low in Al nanostructures compared to Au, particularly due to the destructive effect of the IT, the intensity can be increased by adjusting the shape of the structures. Furthermore, Al dimers are expected to be a promising structure for increasing the near-field intensity up to a hundred-fold compared to a single particle.

We propose that Al nanostructures could potentially be used for the creation of a new generation of solar energy systems, such as transparent solar cells. Indeed, transparency in high-density arrays can be adjusted to simultaneously absorb light in the UV and near-IR regions, with a minimum interaction in the visible window. Moreover, a high absorption-to-scattering ratio and strong near-field enhancement can be achieved with optimized thin, narrow Al rods. This makes them ideal candidates for photocurrent generation as absorption and near-field enhancement are key points to generate hot electrons.[54,55]

■ ASSOCIATED CONTENT

Ⓢ Supporting Information

Figure S1, raw absorption and scattering of Al nanorods as a function of their aspect ratio and thickness; Figure S2, scattering-to-absorption difference as a function of aspect ratio and thickness calculated for Au nanorods; Figure S3, peak position evolution of the two hybrid modes resulting from the LSPR-IT coupling as a function of the aspect ratio; Figure S4, details of the measurements and operations performed to corrected the nonlinearity on PEEM near-field spectra; Figure S5, effect of the Al native oxide on far-field and near-field optical response; Figure S6, evolution of the near-field enhancement as a function of the aspect ratio; Figure S7, experimental and theoretical preliminary results on Al dimers. Experimental details concerning with nanorod fabrication process, optical analysis, PEEM analysis, and FDTD calculations were also provided. This material is available free of charge via the Internet at http://pubs.acs.org.

■ AUTHOR INFORMATION

Corresponding Author
*E-mail: misawa@es.hokudai.ac.jp. Phone: +81-11-706-9358. Fax: +81-11-706-9359.

Notes
The authors declare no competing financial interest.

■ ACKNOWLEDGMENTS

■ REFERENCES

(1) Vo-Dinh, T. *Biomedical Photonics Handbook*; CRC Press: New York, 2003; p 1872.

(2) Qian, X.; Peng, X.-H.; Ansari, D. O.; Yin-Goen, Q.; Chen, G. Z.; Shin, D. M.; Yang, L.; Young, A. N.; Wang, M. D.; Nie, S. In Vivo Tumor Targeting and Spectroscopic Detection with Surface-Enhanced Raman Nanoparticle Tags. *Nat. Biotechnol.* **2008**, *26*, 83−90.

(3) Gobin, A. M.; Lee, M. H.; Halas, N. J.; James, W. D.; Drezek, R. A.; West, J. L. Near-Infrared Resonant Nanoshells for Combined Optical Imaging and Photothermal Cancer Therapy. *Nano Lett.* **2007**, *7*, 1929−1934.

(4) Lal, S.; Clare, S. E.; Halas, N. J. Nanoshell-Enabled Photothermal Cancer Therapy: Impending Clinical Impact. *Acc. Chem. Res.* **2008**, *41*, 1842−1851.

(5) Huang, X.; Jain, P. K.; El-Sayed, I. H.; El-Sayed, M. A. Plasmonic Photothermal Therapy (PPTT) Using Gold Nanoparticles. *Lasers Med. Sci.* **2008**, *23*, 217−228.

(6) Gueymard, C. A. The Sun's Total and Spectral Irradiance for Solar Energy Applications and Solar Radiation Models. *Sol. Energy* **2004**, *76*, 423−453.

(7) Pillai, S.; Catchpole, K. R.; Trupke, T.; Green, M. A. Surface Plasmon Enhanced Silicon Solar Cells. *J. Appl. Phys.* **2007**, *101*, 093105.

(8) Pillai, S.; Green, M. A. Plasmonics for Photovoltaic Applications. *Sol. Energy Mater. Sol. Cells* **2010**, *94*, 1481−1486.

(9) Ferry, V. E.; Munday, J. N.; Atwater, H. A. Design Considerations for Plasmonic Photovoltaics. *Adv. Mater.* **2010**, *22*, 4794−4808.

(10) Nishijima, Y.; Ueno, K.; Yokota, Y.; Murakoshi, K.; Misawa, H. Plasmon-Assisted Photocurrent Generation from Visible to Near-Infrared Wavelength Using a Au-Nanorods/TiO$_2$ Electrode. *J. Phys. Chem. Lett.* **2010**, *1*, 2031−2036.

(11) Nishijima, Y.; Ueno, K.; Kotake, Y.; Murakoshi, K.; Inoue, H.; Misawa, H. Near-Infrared Plasmon-Assisted Water Oxidation. *J. Phys. Chem. Lett.* **2012**, *3*, 1248−1252.

(12) Chan, G. H.; Zhao, J.; Schatz, G. C.; van Duyne, R. P. Localized Surface Plasmon Resonance Spectroscopy of Triangular Aluminum Nanoparticles. *J. Phys. Chem. C* **2008**, *112*, 13958−13963.

(13) Langhammer, C.; Schwind, M.; Kasemo, B.; Zorić, I. Localized Surface Plasmon Resonances in Aluminum Nanodisks. *Nano Lett.* **2008**, *8*, 1461−1871.

(14) Ekinci, Y.; Solak, H. H.; Löffler, J. F. Plasmon Resonances of Aluminum Nanoparticles and Nanorods. *J. Appl. Phys.* **2008**, *104*, 083107.

(15) Zorić, I.; Zäch, M.; Kasemo, B.; Langhammer, C. Gold, Platinum, and Aluminum Nanodisk Plasmons: Material Independence, Subradiance, and Damping Mechanisms. *ACS Nano* **2011**, *5*, 2535−2546.

(16) Knight, M. W.; Liu, L.; Wang, Y.; Brown, L.; Mukherjee, S.; King, N. S.; Everitt, H. O.; Nordlander, P.; Halas, N. J. Aluminum Plasmonic Nanoantennas. *Nano Lett.* **2012**, *12*, 6000−6004.

(17) Taguchi, A.; Saito, Y.; Watanabe, K.; Yijian, S.; Kawata, S. Tailoring Plasmon Resonances in the Deep-Ultraviolet by Size-Tunable Fabrication of Aluminum Nanostructures. *Appl. Phys. Lett.* **2012**, *101*, 081110.

(18) Maidecchi, G.; Gonella, G.; Zaccaria, R. P. Deep Ultraviolet Plasmon Resonance in Aluminum Nanoparticle Arrays. *ACS Nano* **2013**, *7*, 5834−5841.

(19) Ehrenreich, H.; Philipp, H.; Segall, B. Optical Properties of Aluminum. *Phys. Rev.* **1963**, *132*, 1918.

(20) Villesen, T. F.; Uhrenfeldt, C.; Johansen, B.; Nylandsted Larsen, A. Self-Assembled Al Nanoparticles on Si and Fused Silica, and Their Application for Si Solar Cells. *Nanotechnology* **2013**, *24*, 275606.

(21) Villesen, T. F.; Uhrenfeldt, C.; Johansen, B.; Hansen, J. L.; Ulriksen, H. U.; Larsen, A. N. Aluminum Nanoparticles for Plasmon-Improved Coupling of Light into Silicon. *Nanotechnology* **2012**, *23*, 085202.

(22) Hylton, N. P.; Li, X. F.; Giannini, V.; Lee, K.-H.; Ekins-Daukes, N. J.; Loo, J.; Vercruysse, D.; van Dorpe, P.; Sodabanlu, H.; Sugiyama, M.; Maier, S. A. Loss Mitigation in Plasmonic Solar Cells: Aluminium Nanoparticles for Broadband Photocurrent Enhancements in GaAs Photodiodes. *Sci. Rep.* **2013**, *3*, 2874.

(23) Schwind, M.; Kasemo, B.; Zorić, I. Localized and Propagating Plasmons in Metal Films with Nanoholes. *Nano Lett.* **2013**, *13*, 1743−1750.

(24) Bobbert, P. A.; Vlieger, J. Light Scattering by a Sphere on a Substrate. *Phys. A (Amsterdam, Neth.)* **1986**, *137*, 209−242.

(25) Curry, A.; Nusz, G.; Chilkoti, A.; Wax, A. Substrate Effect on Refractive Index Dependence of Plasmon Resonance for Individual Silver Nanoparticles Observed Using Darkfield Microspectroscopy. *Opt. Express* **2005**, *13*, 2668.

(26) Knight, M. W.; Wu, Y.; Lassiter, J. B.; Nordlander, P.; Halas, N. J. Substrates Matter: Influence of an Adjacent Dielectric on an Individual Plasmonic Nanoparticle. *Nano Lett.* **2009**, *9*, 2188−2192.

(27) Auguié, B.; Barnes, W. Collective Resonances in Gold Nanoparticle Arrays. *Phys. Rev. Lett.* **2008**, *101*, 1−4.

(28) Chu, Y.; Schonbrun, E.; Yang, T.; Crozier, K. B. Experimental Observation of Narrow Surface Plasmon Resonances in Gold Nanoparticle Arrays. *Appl. Phys. Lett.* **2008**, *93*, 181108.

(29) Su, K.-H.; Wei, Q.-H.; Zhang, X.; Mock, J. J.; Smith, D. R.; Schultz, S. Interparticle Coupling Effects on Plasmon Resonances of Nanogold Particles. *Nano Lett.* **2003**, *3*, 1087−1090.

(30) Atay, T.; Song, J.-H.; Nurmikko, A. V. Strongly Interacting Plasmon Nanoparticle Pairs: From Dipole−Dipole Interaction to Conductively Coupled Regime. *Nano Lett.* **2004**, *4*, 1627−1631.

(31) Nordlander, P.; Oubre, C.; Prodan, E.; Li, K.; Stockman, M. I. Plasmon Hybridization in Nanoparticle Dimers. *Nano Lett.* **2004**, *4*, 899−903.

(32) Lecarme, O.; Pinedo-Rivera, T.; Berton, K.; Berthier, J.; Peyrade, D. Plasmonic Coupling in Nondipolar Gold Colloidal Dimers. *Appl. Phys. Lett.* **2011**, *98*, 83122.

(33) Jain, P. K.; El-Sayed, M. A. Plasmonic Coupling in Noble Metal Nanostructures. *Chem. Phys. Lett.* **2010**, *487*, 153−164.

(34) Rechberger, W.; Hohenau, A.; Leitner, A.; Krenn, J. R.; Lamprecht, B.; Aussenegg, F. R. Optical Properties of Two Interacting Gold Nanoparticles. *Opt. Commun.* **2003**, *220*, 137−141.

(35) Khunsin, W.; Brian, B.; Dorfmüller, J.; Esslinger, M.; Vogelgesang, R.; Etrich, C.; Rockstuhl, C.; Dmitriev, A.; Kern, K. Long-Distance Indirect Excitation of Nanoplasmonic Resonances. *Nano Lett.* **2011**, *11*, 2765−2769.

(36) Rakić, A. D. Algorithm for the Determination of Intrinsic Optical Constants of Metal Films: Application to Aluminum. *Appl. Opt.* **1995**, *34*, 4755.

(37) Kreibig, U.; Vollmer, M. *Optical Properties of Metal Clusters*; Springer: New York, 1995.

(38) Pakizeh, T. Optical Absorption of Plasmonic Nanoparticles in Presence of a Local Interband Transition. *J. Phys. Chem. C* **2011**, *115*, 21826−21831.

(39) Zeman, E. J.; Schatz, G. C. An Accurate Electromagnetic Theory Study of Surface Enhancement Factors for Silver, Gold, Copper, Lithium, Sodium, Aluminum, Gallium, Indium, Zinc, and Cadmium. *J. Phys. Chem.* **1987**, *91*, 634−643.

(40) Bohren, C. F.; Huffman, D. R. *Absorption and Scattering of Light by Small Particles*; Wiley: New York, 1998.

(41) Bréchignac, C.; Houdy, P.; Lahmani, M. *Nanomaterials and Nanochemistry*; Springer: New York, 2007.

(42) Sönnichsen, C.; Franzl, T.; Wilk, T.; von Plessen, G.; Feldmann, J. Drastic Reduction of Plasmon Damping in Gold Nanorods. *Phys. Rev. Lett.* **2002**, *88*, 77402.

(43) Kubo, A.; Onda, K.; Petek, H.; Sun, Z.; Jung, Y. S.; Kim, H. K. Femtosecond Imaging of Surface Plasmon Dynamics in a Nanostructured Silver Film. *Nano Lett.* **2005**, *5*, 1123−1127.

(44) Douillard, L.; Charra, F.; Fiorini, C.; Adam, P. M.; Bachelot, R.; Kostcheev, S.; Lerondel, G.; Lamy de la Chapelle, M.; Royer, P. Optical Properties of Metal Nanoparticles as Probed by Photoemission Electron Microscopy. *J. Appl. Phys.* **2007**, *101*, 083518.

(45) Sun, Q.; Ueno, K.; Yu, H.; Kubo, A.; Matsuo, Y.; Misawa, H. Direct Imaging of the near Field and Dynamics of Surface Plasmon Resonance on Gold Nanostructures Using Photoemission Electron Microscopy. *Light Sci. Appl.* **2013**, *2*, e118.

(46) Knight, M. W.; King, N. S.; Liu, L.; Everitt, H. O.; Nordlander, P.; Halas, N. J. Aluminum for Plasmonics. *ACS Nano* **2013**, *7*, 2388−2395.

(47) Abboud, J. E.; Chong, X.; Zhang, M.; Zhang, Z.; Jiang, N.; Roy, S.; Gord, J. R. Photothermally Activated Motion and Ignition Using Aluminum Nanoparticles. *Appl. Phys. Lett.* **2013**, *102*, 023905.

(48) Dintinger, J.; Klein, S.; Bustos, F.; Barnes, W.; Ebbesen, T. Strong Coupling between Surface Plasmon-Polaritons and Organic Molecules in Subwavelength Hole Arrays. *Phys. Rev. B* **2005**, *71*, 035424.

(49) Fofang, N. T.; Grady, N. K.; Fan, Z.; Govorov, A. O.; Halas, N. J. Plexciton Dynamics: Exciton-Plasmon Coupling in a J-Aggregate-Au Nanoshell Complex Provides a Mechanism for Nonlinearity. *Nano Lett.* **2011**, *11*, 1556−1160.

(50) Schlather, A. E.; Large, N.; Urban, A. S.; Nordlander, P.; Halas, N. J. Near-Field Mediated Plexcitonic Coupling and Giant Rabi Splitting in Individual Metallic Dimers. *Nano Lett.* **2013**, *13*, 3281−3286.

(51) Xu, H.; Aizpurua, J.; Käll, M.; Apell, P. Electromagnetic Contributions to Single-Molecule Sensitivity in Surface-Enhanced Raman Scattering. *Phys. Rev. E* **2000**, *62*, 4318−4324.

(52) Hatab, N. A.; Hsueh, C.-H.; Gaddis, A. L.; Retterer, S. T.; Li, J.-H.; Eres, G.; Zhang, Z.; Gu, B. Free-Standing Optical Gold Bowtie Nanoantenna with Variable Gap Size for Enhanced Raman Spectroscopy. *Nano Lett.* **2010**, *10*, 4952−4955.

(53) Seok, T. J.; Jamshidi, A.; Kim, M.; Dhuey, S.; Lakhani, A.; Choo, H.; Schuck, P. J.; Cabrini, S.; Schwartzberg, A. M.; Bokor, J.; et al. Radiation Engineering of Optical Antennas for Maximum Field Enhancement. *Nano Lett.* **2011**, *11*, 2606−2610.

(54) Linic, S.; Christopher, P.; Ingram, D. B. Plasmonic-Metal Nanostructures for Efficient Conversion of Solar to Chemical Energy. *Nat. Mater.* **2011**, *10*, 911−921.

(55) Sheehan, S. W.; Noh, H.; Brudvig, G. W.; Cao, H.; Schmuttenmaer, C. a. Plasmonic Enhancement of Dye-Sensitized Solar Cells Using Core−Shell−Shell Nanostructures. *J. Phys. Chem. C* **2013**, *117*, 927−934.